Thin accretion discs around spherically symmetric configurations with nonlinear scalar fields

O. S. Stashko, V. I. Zhdanov, and A. N. Alexandrov
Astronomical Observatory, Taras Shevchenko National University of Kyiv, UA-01033 Kyiv, Ukraine

(Received 18 July 2021; accepted 5 October 2021; published 23 November 2021)

We study stable circular orbits (SCO) around static spherically symmetric configuration of general relativity with a nonlinear scalar field (SF). The configurations are described by solutions of the Einstein-SF equations with monomial SF potential $V(\phi) = |\phi|^{2n}$, $n > 2$, under the conditions of the asymptotic flatness and behavior of SF $\phi \sim 1/r$ at spatial infinity. We proved that under these conditions, the solution exists and is uniquely defined by the configuration mass $M > 0$ and scalar "charge" Q. The solutions and the space-time geodesics have been investigated numerically in the range $n \leq 40$, $|Q| \leq 60$, $M \leq 60$. We focus on how nonlinearity of the field affects properties of SCO distributions (SCOD), which, in turn, affect topological form of the thin accretion disk around the configuration. Maps are presented showing the location of possible SCOD types for different M, Q, n. We found a lot of differences from the Fisher-Janis-Newman-Winicour metric (FJNW) dealing with the linear SF, though basic qualitative properties of the configurations have much in common with the FJNW case. For some values of n, a topologically new SCOD type was discovered that is not available for the FJNW metric. Like FJNW, all images of accretion disks have a dark spot in the center (mimicking the ordinary black hole), either because there is no SCO near the center or due to the strong deflection of photons near the singularity, although fine features other than a black hole can appear with a special choice of M, Q.

DOI: 10.1103/PhysRevD.104.104055

I. INTRODUCTION

Scalar field (SF) configurations in general relativity and its modifications are interesting for several reasons. Various SF models are extensively used in cosmology [1–4]. Some propositions to relax the well-known "Hubble tension" involve SF in diverse approaches to dynamical dark energy (see [5] for a review). It is currently unknown, whether the cosmological fields of the late epoch (if any) are the same as the fields that caused the early inflation or they are of a completely different nature. In any case, the question arises about possible manifestations of SF in relativistic astrophysical objects. Interest in alternative models of these objects has increased significantly after the image of the accretion disk in the core of M87 had been obtained with the Event Horizon Telescope (EHT) [6], demonstrating future prospects to distinguish the black holes from their exotic mimickers.

The first example of the static spherically symmetric solution of Einstein equations with linear massless SF has been found by Fisher [7] and later, in the other form, by Janis, Newman, and Winicour [8] (hereinafter, FJNW; see also [9,10]). The FJNW metric does not describe a black hole (BH); it has naked singularity (NS) in the center not hidden by an event horison. This is a typical feature of static solutions with SF describing compact objects due to the Bekenstein theorems [11,12]; see also a generalization in case of multiple SFs [13]. The occurrence of NS in the real Universe is forbidden by the Penrose Cosmic Censorship hypothesis [14,15], though the question on the validity of this hypothesis remains open [16–19]. Current discussions on this topic have shifted to issues of stability and realistic choices of initial data for the gravitational collapse that may or may not lead to NS (see, e.g., [20] for a review).

Anyway, the final answer regarding the role of SF in astrophysics must be based on observations. It should be noted that there are "exotic" structures [21–28], which mimic the BHs yielding image similar to that observed by EHT [6]. New theoretical efforts as well as observations with better resolution are mandatory. Given the progress in astronomical technology, it is important to study in detail the properties of relativistic astrophysical objects, which can help to select the appropriate options from a variety of theoretical models. The main source of observational information from these objects is associated with the distribution of surrounding radiating matter (accretion disks, jets, etc.) and images of this matter seen by a distant observer. The very first step is to study stable circular orbits (SCO) of test bodies and their distribution in a gravitational field of the configuration. There are a number of papers on this subject including those, which use FJNW solution dealing with the linear SF [27,29–34], and it would be interesting to study effects of nonlinearity. Several examples [33,35–42] demonstrate occurrence of circular orbit

distributions with several nonconnected rings of SCO. This may be of particular interest as observational signs of differences from ordinary black holes, as well as the unusual form of the accretion disk images and/or their radiation properties [19,19,24,30–32,43–48].

In the present paper, we will look for the effects of nonlinear fields on the SCO distribution (SCOD) around the center. For this purpose, we consider SFs determined by a sequence of monomial potentials $V(\phi) = \phi^{2n}$, $n > 2$, which have a simple asymptotic behavior $\phi(r) \sim 1/r$ at large distances (analogous to FJNW).[1] The reason for such a choice is that this is the simplest nonlinear generalization of the FJNW problem. On the other hand, the monomial potentials are often used in various cosmological problems (see, e.g., [49–51]). We numerically obtain static solutions of the Einstein-SF equations in the case of spherical symmetry and use these results to study SCO with focus on the qualitative features of SCOD, as well as on images of these distributions that can be observed from infinity. Namely, we systematically analyze the permitted SCO regions.

The paper is organized as follows. In Sec. II, we write down the basic equations and integrate them numerically. The use of numerical methods presupposes that the problem is well posed. In this regard, we rely on the results of [52], which guarantee that our solutions are regular, and they have no singularities outside the center (in contrast, e.g., to some special relativistic cases [52]). Also, in Appendix, we prove that there is a unique solution defined by the boundary conditions at infinity. In Sec. III, we proceed to test particle motion in the gravitational field of the configuration, the "equatorial" plane, and present possible SCOD. Four qualitatively different SCOD types are introduced, differing in the number of individual SCO rings (Sec. III B). Here, we demonstrate how the topology of the SCO rings change with n and present maps that define types of SCOD for given configuration parameters. Section III C discusses photon trajectories that are used to build the images of different SCOD. The concluding remarks are summarized in Sec. IV where we discuss observational signatures of SCOD, which can be used to distinguish them.

II. SPHERICALLY SYMMETRIC STATIC SOLUTIONS OF EINSTEIN RELATIONS WITH SCALAR FIELD

The general metric of a static spherically symmetric space-time in the curvature coordinates (Schwarzschild-like) is

$$ds^2 = e^{\alpha(r)}dt^2 - e^{\beta(r)}dr^2 - r^2dO^2, \tag{1}$$

where $dO^2 = d\theta^2 + (\sin\theta)^2 d\varphi^2$; the radial variable $r > 0$.

We consider one minimally coupled real SF ϕ with Lagrangian density,

$$L = \frac{1}{2}\phi_{,\mu}\phi^{,\mu} - V(\phi), \tag{2}$$

with

$$V(\phi) = |\phi|^{2n}, \quad n > 2, \tag{3}$$

where n is not necessarily an integer. More general power law potential can be reduced to (3) by rescaling of the variables. Note that for $V(\phi) = 0$ we have the well known FJNW solution. Some results concerning cases $1 \le n < 2$ can be found in [52–55].

The Einstein-SF equations are reduced to the following system:

$$\frac{d}{dr}[r(e^{-\beta} - 1)] = -8\pi r^2[e^{-\beta}\phi'^2/2 + V(\phi)], \tag{4}$$

where $\phi \equiv \phi(r)$,

$$re^{-\beta}\frac{d\alpha}{dr} + e^{-\beta} - 1 = 8\pi r^2[e^{-\beta}\phi'^2/2 - V(\phi)], \tag{5}$$

and

$$\frac{d}{dr}\left[r^2 e^{\frac{\alpha-\beta}{2}}\frac{d\phi}{dr}\right] = r^2 e^{\frac{\alpha+\beta}{2}}V'(\phi). \tag{6}$$

Here, $\alpha(r), \beta(r)$ are assumed to be C^1 functions, and $\phi(r)$ is a C^2 function for $r > 0$.

We deal with isolated configurations; correspondingly, we impose the asymptotic flatness conditions as follows:

$$\lim_{r\to\infty}[r(e^{\alpha} - 1)] = \lim_{r\to\infty}[r(e^{-\beta} - 1)] = -r_g, \tag{7}$$

where $r_g = 2M$ and $M > 0$ is the configuration mass; also, $\phi(r) \to 0$ for $r \to \infty$, and

$$\lim_{r\to\infty} r^2\frac{d\phi}{dr} = -Q, \tag{8}$$

where parameter Q determines asymptotics of the field at spatial infinity; we will call it "scalar charge." Relation (8) yields

$$\lim_{r\to\infty} r\phi(r) = Q.$$

The global behavior of the solutions satisfying (7) and (8) has been studied in a more general case of multiple scalar fields [52], where a proof of regularity of solutions

[1]The cases with $n \le 2$ lead to asymptotics at infinity different from $\sim 1/r$.

on an open interval $(0, \infty)$ is given. Asymptotic properties for $r \to \infty$ have been derived in [52] for a particular case, under the assumption that the solutions can be expanded in powers of $1/r$. In Appendix of the present paper, we provide a more rigorous analysis by means of an iteration procedure. We prove that there is a solution of equations (4), 6) ,(5)) for $r \geq r_{\rm in}$, where $r_{\rm in}$ is large enough, with the conditions (8); this solution is uniquely defined by parameters M, Q. The first iterations of this procedure yield asymptotic relations for large r as follows:

$$\phi(r) = \frac{Q}{r}\left[1 + \frac{r_g}{2r} + \frac{n|Q|^{2n-2}}{(n-2)(2n-3)r^{2n-4}}\right] + O\left[\frac{\mu(r)}{r^2}\right], \quad (n > 2), \tag{9}$$

$$e^{\alpha} = \left(1 - \frac{r_g}{r}\right)\left[1 + O\left(\frac{\mu(r)}{r^2}\right)\right],$$

$$e^{-\beta} = \left(1 - \frac{r_g}{r}\right)\left[1 + \frac{4\pi Q^2}{r^2} + O\left(\frac{\mu(r)}{r^2}\right)\right], \tag{10}$$

where $\mu(r) = 1/r$ for $n \geq 3$ and $\mu(r) = 1/r^{2n-4}$ for $2 < n < 3$. Note that in the general case, (9) and (10) can contain noninteger powers of $1/r$.

Asymptotics of the metric near the center can be found in [52]: $\alpha(r) \sim (\eta - 1)\ln r$, $\beta(r) \sim (\eta + 1)\ln r$. Parameter η characterizes the strength of the singularity. There is a critical point $\eta = 3$ that separates two types of the singularity with different behavior of the null geodesics (see below).

We performed a detailed numerical investigation of the problem (4)–(8) for $n \leq 40$, $M \leq 60$, $|Q| \leq 60$. To find the solutions for $r \leq r_{\rm in}$, we proceed numerically starting at sufficiently large initial radius $r_{\rm in}$ (up to 10^5) to use initial conditions in accordance with asymptotic relations (9), (10). We integrate backward from higher to lower values of $r \in (0, r_{\rm in}]$. The qualitative properties of the metric coefficients and scalar field are rather similar for different values of parameters (Q, M, n): $\alpha(r)$ is a monotonically increasing function bounded from above by 1 for $r \to \infty$ and $\beta(r)$, has a maximum at some point $r = r_{\rm max}(Q)$. If Q increases, then $r_{\rm max}(Q)$ is shifted to larger values, and the maximum becomes less pronounced. The scalar field is always a monotonically decreasing function, and $\phi \to 0$ as $r \to \infty$. For large n and fixed M, Q, the solutions approach the FJNW curves, except for a small region near the singularity. An important point is the dependence of η upon the parameters of the configuration at spatial infinity. Qualitatively, dependencies $\eta(M, Q)$ for different n are rather similar; Fig. 1 shows the examples for $n = 3$ and $n = 14$.

III. TEST PARTICLE MOTION

A. General relations

This section deals with trajectories of the test particles in the space-time corresponding to the solutions of the problem (4)–(8). The equations of the test particle motion follow from formal Lagrangian,

$$L = g_{\mu\nu}\frac{dx^{\mu}}{d\tau}\frac{dx^{\nu}}{d\tau}, \tag{11}$$

where τ is a canonical parameter. Standard procedure involves the first integrals for trajectories in the equatorial plane $(\theta = \pi/2)$:

$$e^{\alpha}\left(\frac{dt}{d\tau}\right)^2 - e^{\beta}\left(\frac{dr}{d\tau}\right)^2 - r^2\left(\frac{d\varphi}{d\tau}\right)^2 = S, \tag{12}$$

$$e^{\alpha}\left(\frac{dt}{d\tau}\right) = E, \qquad r^2\left(\frac{d\varphi}{d\tau}\right) = L, \tag{13}$$

where $S = 0$ in case of null trajectories, and $S = 1$ for the test particles with the nonzero mass; L, E are the integrals of motion. This yields

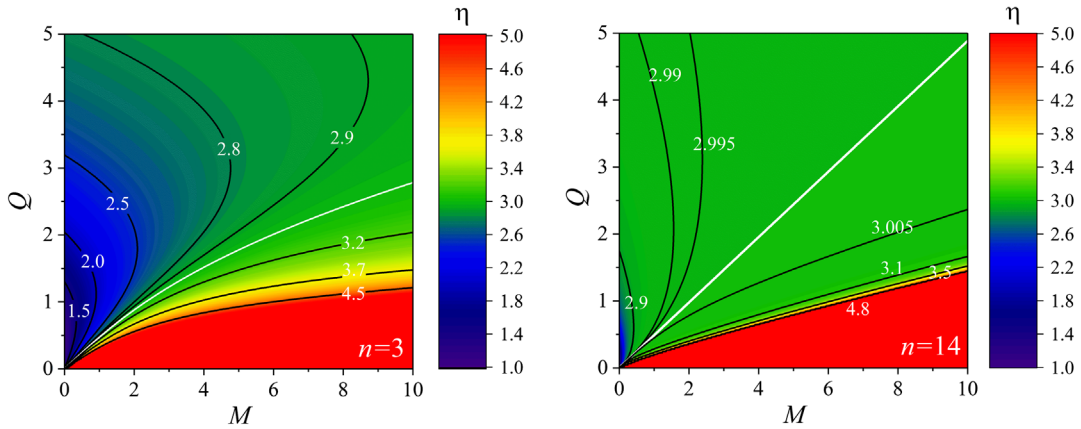

FIG. 1. Contours of the equal η as function of M, Q for $n = 3$ (left panel) and $n = 14$ (right panel). The solid white line corresponds to critical value $\eta = 3$. If $Q \to 0$, then $\eta \to \infty$.

$$e^{\alpha+\beta}\left(\frac{dr}{d\tau}\right)^2 = E^2 - U_{\rm eff}(r, L, S), \tag{14}$$

where $U_{\rm eff}(r, L, S) = e^{\alpha}(S + L^2/r^2)$.

Thus, the problem is reduced to investigation of the one-dimensional particle motion in the field of effective potential $U_{\rm eff}$. The asymptotic behavior of the potential depends on asymptotics (10) at infinity and those near singularity (see [52]). For $L \neq 0$, we have

$$U_{\rm eff}(r \to 0) \sim r^{\eta-3}, \qquad U_{\rm eff}(r \to \infty) \to S. \tag{15}$$

Thus, for $\eta < 3$, we have $U_{\rm eff} \to \infty$ at $r \to 0$; i.e., there is an infinite potential barrier that will reflect falling particles. For $\eta > 3$, $U_{\rm eff} \to 0$ at $r \to 0$, the particles can approach the center, and there is a maximum at some $r_u > 0$, which is the radius of an unstable circular orbit.

B. Circular orbits

We consider the Page-Thorne model of the geometrically thin accretion disk (AD) [56], where the averaged motion of accretion matter is approximated by means of SCO around gravitating center. A circular orbit is stable if the right-hand side of (14) is zero, and $dU_{\rm eff}/dr$ changes its sign at this point. For the congruence of circular orbits with different radii in equatorial plane, we get dependencies of the specific energy and the specific angular momentum, and the angular velocity $\Omega = d\varphi/dt$ upon radius r as follows:

$$\tilde{E}^2(r) = \frac{2e^{\alpha(r)}}{2 - r\alpha'(r)}, \qquad \tilde{L}^2(r) = \frac{r^3\alpha'(r)}{2 - r\alpha'(r)},$$
$$\Omega^2(r) = \frac{\alpha'(r)e^{\alpha(r)}}{2r}. \tag{16}$$

We use the method of works [41,57] to study bifurcations associated with the appearance and disappearance of the minima of $U_{\rm eff}$. Essentially, this is connected with the investigation of joint conditions $U'_{\rm eff} = 0$ and $U''_{\rm eff} = 0$, which allow us to exclude L; this leads to a necessary condition $F(r) = 0$, where

$$F(r) = \tilde{L}^2(r)[r^2\alpha''(r) - 2r\alpha'(r) + 6] + r^4\alpha''(r). \tag{17}$$

Using Eq. (17), we get the bifurcation values r_b, $L_b^2 = \tilde{L}^2(r_b)$ and $E_b^2 = \tilde{E}^2(r_b)$ under conditions that $\tilde{E}^2(r_b) > 0$ and $\tilde{L}^2(r_b) > 0$. We tested our results by considering the explicit forms of $U_{\rm eff}$ near the bifurcations as in the example in Fig. 2. The right panel of Fig. 2 illustrates occurrence of three minima (which is not observed in case of FJNW solution); it shows how the shape of the potential changes with increasing the angular momentum, and as a result, the third minimum appears in the vicinity of the singularity. Note that the bifurcation radius (boundary radius), signalizing emergence or disappearance of some minimum of $U_{\rm eff}$, indicates the boundary of some SCO ring for a given configuration.

The above reasoning allowed us to obtain the boundaries of rings containing SCO, which are separated by regions where circular orbits are either unstable or do not exist. Figures 3, 4, and 5 below present examples of bifurcation curves, which define these boundaries.

Here, we describe main results of our numerical investigation of the bifurcation radii $r_b \equiv r_{i(T)}$, where index T denotes various SCOD type explained below. We show that at least four SCOD types are possible in our problem.

The next three types deal with the case of $\eta < 3$ (effective potentials are unbounded).

(i) $S1$: $\tilde{L}(r)$ is monotonically increasing function. As a result, we have one connected domain of SCO with radii $r \in (0, \infty)$. SCO fill all the space.

(ii) $S2$: The effective potentials $U_{\rm eff}$ have two minima, which correspond to the SCO radii. As a result, we have the inner disk with SCO radii $r \in (0, r_{1(2)})$ and

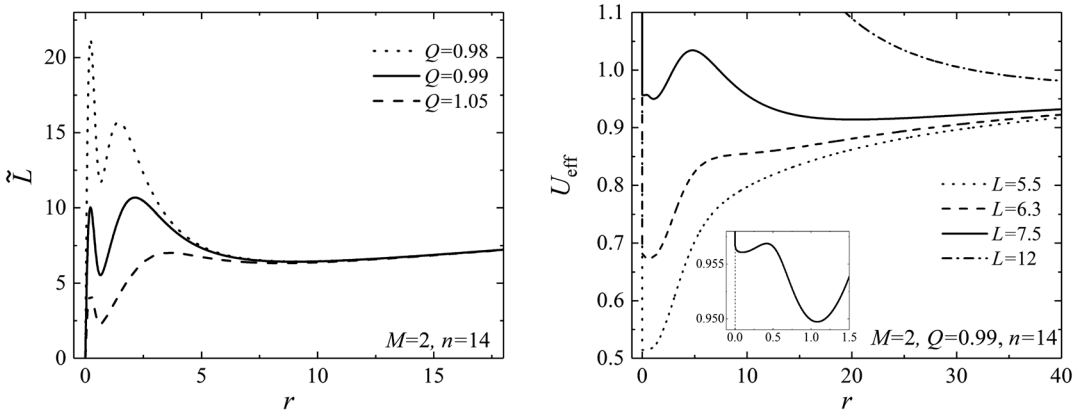

FIG. 2. Typical dependencies $\tilde{L}(r)$ and $U_{\rm eff}(r)$ in the case of $S3$ type; $\eta < 3$ and $U_{\rm eff}(r)$ is infinite for $r \to 0$. The left panel shows that there can exist several circular orbits with the same $\tilde{L}(r) = L$. Roots of this equation correspond to SCO if they belong to the intervals where $\tilde{L}'(r) > 0$. The right panel shows effective potential with three minima ($S3$ type). Three different SCO rings can exist near $L \sim 6.3$ and about fixed M, Q, n indicated in the figure.

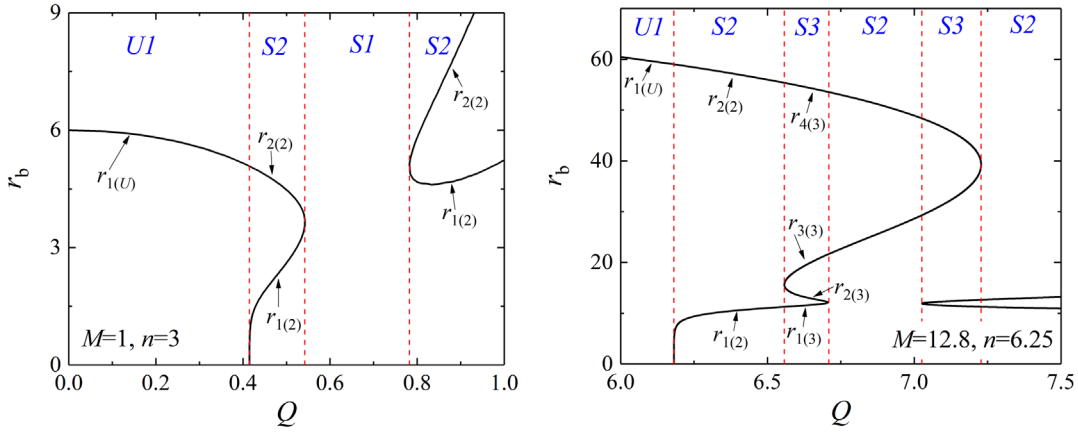

FIG. 3. Boundary radii of SCO regions as a function of Q for some fixed M, n. Vertical dashed lines separate areas of different SCOD types. In the left panel, we have the $S1$ area between two branches of the bifurcation curve; here, arbitrary SCO radii are allowed. The other allowed region of radii are according to definition of $U1$ and $S2$. The right panel shows the example with larger M, Q, n, when another type is present, namely $S3$; corresponding parameters fall into the yellow region on Figs. 8–11.

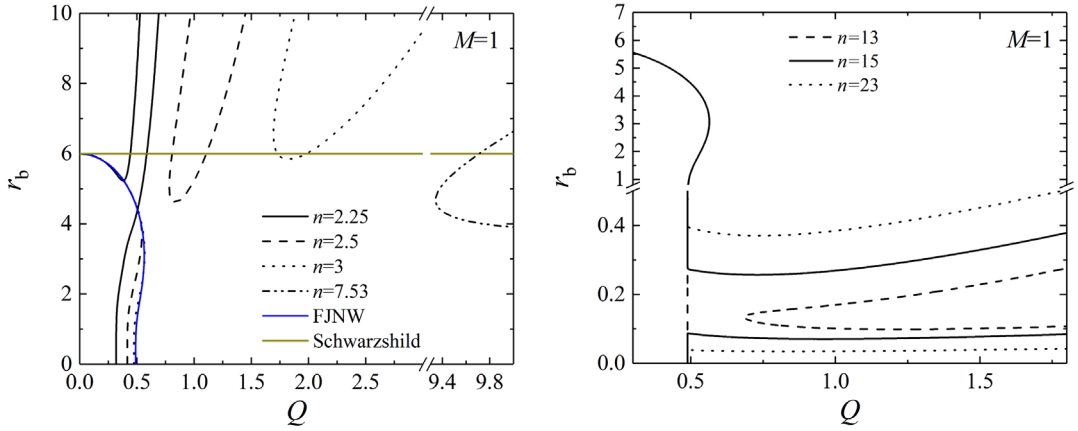

FIG. 4. Boundary radii r_b of SCO regions as a functions of Q for $M = 1$ and several fixed values of n. The continuous blue line on the left panel represents the FJNW solution and the orange straight line corresponds to the Schwarzschild BH case ($r_{\mathrm{ISCO}} = 6M$). The first reshaping occurs at $n_1^* \approx 2.38$; then the right branch moves to the right and then starts backtracking to the left branch when $n > n_2^* \approx 7.53$. We found $n_3^* \approx 13.12$ and $n_4^* \approx 13.13$. For $n \geq n_5^* \approx 13.15$, the form of the branches is represented by solid ($n = 15$) and dotted ($n = 23$) lines on the right panel; here, we also have the $S3$ type (four-valued function $r_b(Q)$ on some interval of Q).

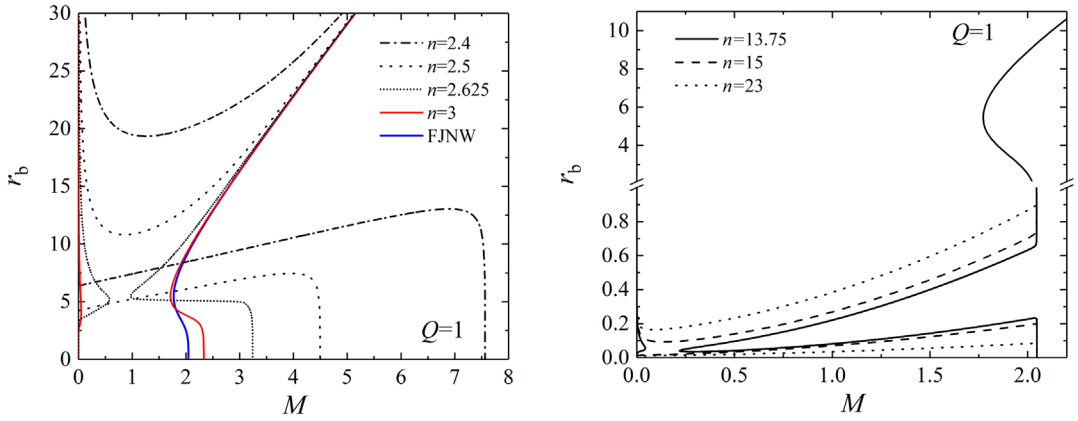

FIG. 5. Boundary radii r_b of SCO regions as a functions of M for $Q = 1$ and several fixed values of n. The first reconnection of two branches occurs at $n \approx 2.62$; dash-dotted ($n = 2.4$) and dotted ($n = 2.5$) lines show the typical form of branches before the reshaping (left panel), and the lines with $n = 2.625$ and $n = 3$ show the typical forms after the reshaping. The right panel demonstrates the branches around the second reconnection near $n \approx 13.86$.

the outer disk with $r \in (r_{2(2)}, \infty)$. Hereinafter, the index in parenthesis denotes the type.

(iii) $S3$: We found a new type of the SCO distribution that does not exist in the FJNW case. The effective potential $U_{\rm eff}$ can have three possible minima and two maxima corresponding to three SCO regions $r \in (0, r_{1(3)})$, $(r_{2(3)}, r_{3(3)})$, $(r_{4(3)}, \infty)$. These regions are separated by two rings of the unstable orbits with $r \in (r_{1(3)}, r_{2(3)})$, $(r_{3(3)}, r_{4(3)})$. Figure 2 shows typical dependencies of $U_{\rm eff}(r, L)$ and $\tilde{L}(r)$. The emergence of SCO with small radii $r < r_{1(3)})$ occurs in a neighborhood of $\eta \sim 3$, where the type of the singularity and the shape of $U_{\rm eff}$ change.

If $\eta \geq 3$, then effective potential has a maximum $U_{\rm eff}(r_{\rm max}, L)$ for any L. There is a region where either there are no circular orbits at all, or they are unstable.

Here, we have only one type:

(i) $U1$ (Schwarzshild-like SCO distribution): The effective potential $U_{\rm eff}$ is bounded from above; $U_{\rm eff} \to 0$ for $r \to 0$ and only one minimum can exist. We have one unstable and one stable regions of SCO; the latter for $r \in (r_{1(U)}, \infty)$ with lower boundary $r_{1(U)}$.

Note that types $U1$, $S1$, $S2$ exist in the FJNW case.

Figure 3 show two illustrative examples of bifurcation radii $r_b(Q) \equiv r_{i(T)}(Q)$, and T means type of SCOD, as a functions of Q, which realize different SCOD types. Figure 4 shows essentially the same, but with more complete picture of the bifurcation radii, which illustrates how the curves transform for larger n values. Analogous dependencies are shown on Fig. 5 as functions on M. Figures 4 and 5 show how the shape of the curves changes when n passes some critical values.

For every M, there are two branches of the curve $r_b(Q)$ (unlike the FJNW case, where there is a single branch exists), and there is a sequence of values $n_1^* < n_2^* < n_3^* < n_4^* < n_5^*$, which has the following properties.

(i) The first and the last values denote critical numbers n_1^*, n_5^*, which correspond to a reshaping (reconnection) of two branches.

(ii) For $2 < n < n_1^*$, both branches are unbounded (like two solid curves on the left panel of Fig. 4). After the reshaping, for $n \in (n_1^*, n_4^*)$ with some $n_4^* > n_1^*$, the left branch comes close to the FJNW curve (practically merges), whereas the right one is unbounded (see dashed and dotted curves on the left panel of Fig. 4).

(iii) For $n_1^* < n < n_2^*$, the right branch moves away to the right and then, for $n > n_2^*$, it starts moving to the left. It is important to note that for moderate $n \lesssim 7$, the sizes of unstable regions can be noticeably larger than in the FJNW case.

(iv) At $n = n_3^*$, an additional wedge-shaped feature in the left branch appears. This is difficult to show in the right panel of Fig. 4 for $M = 1$, but this is well seen for larger M, Q in the right panel of Fig. 3: The corresponding feature is formed by sections $r_{1(3)}$ and $r_{2(3)}$ within the area of $S3$ type. This corresponds to the "Pinocchio's nose" in the right panel of Fig. 5 (solid curve) shown for $n = 13.75$ as the example.

(v) For $n \in (n_4^*, n_5^*)$, the right branch returns closer enough to the left one and a new $S3$ area appears. See the right panel of Fig. 3, where there is an additional small $S3$ area due to the sharp wedge for $r_b \sim 10$, $Q \gtrsim 7$.

(vi) At $n = n_5^*$, the tips of the two wedges (see the right panel of Fig. 3) touch each other. The new reshaping of the bifurcation curve occurs, after which, the branches reconnect forming a structure represented by the solid curve on the right panel of Fig. 4. For large enough n, the lower branch tends to the abscissa axis.

We have determined the number of rings with stable and unstable circular orbits and built maps of possible SCODs in the M–Q plane for different n. Each point on every map (see Figs. 6 and 7) shows the type of SCOD.

For all M and n, there are $S2$ and $U1$ types with appropriate Q. We note that the "thickness" of the ring in the $S1$ case can be considerably larger than in the FJNW case. The size of $S1$ area changes nonmonotonically: It increases up to $n \sim 7$ and then decreases.

We discovered that the $S3$ region emerges for $n \approx 4.32$ (Fig. 6, right); for larger n, this region becomes to appear for smaller M (Fig. 7, right).

C. Photon trajectories and accretion disk images

In case of null geodesics ($S = 0$), the effective potential $U_{\rm eff}(r, L, 0) = e^{\alpha} L^2/r^2$ has simple properties. Its asymptotics are due to (15). The sign of $U_{\rm eff}/dr$ is defined by function,

$$f(r) = r\alpha'(r) - 2. \tag{18}$$

We have verified numerically that $f(r)$ is a monotonically decreasing function; evidently, $f(\infty) = -2$. For $r \to 0$, we have $f(r) \gtrless 0$ if $\eta \gtrless 3$. Therefore, the root of this function can exist only if $\eta > 3$; then the point of maximum $r_{\rm ph}$ is a single root of $f(r)$, $r_{\rm ph}$ being the radius of the photon sphere. Figure 12 shows typical dependencies of the photon orbit's radii on the configuration parameters. One can see that $r_{\rm ph}$ is always less than the corresponding radius in Schwarzshild/FJNW cases.

The next step in the study of the configurations in question concerns the images of accretion discs represented by different types of SCOD. In order to build direct accretion disk images, we use the ray-tracing algorithm described in [58–60]. The complete consideration of this problem requires knowledge of the surface brightness

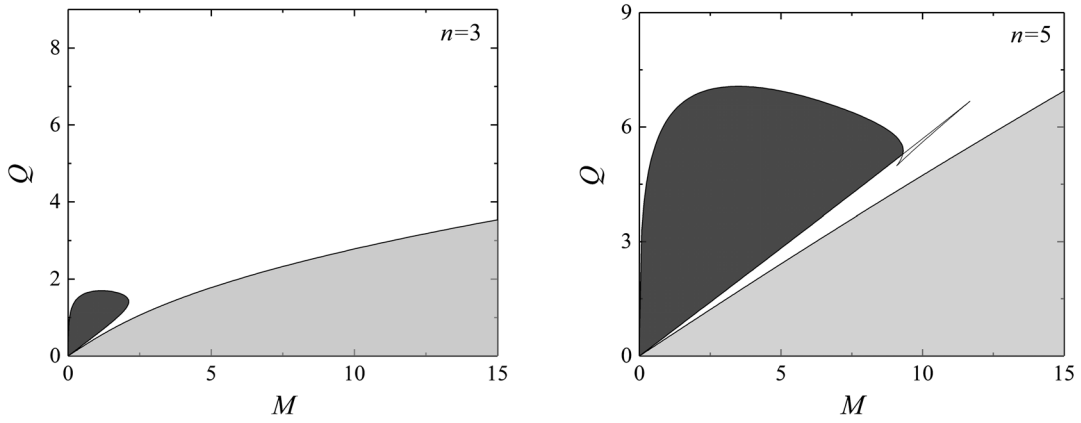

FIG. 6. Domains of parameters on (M, Q) plane for different values of n. Here and on figures below, white color denotes the $S2$ type, yellow-$S3$, light gray-$U1$, dark gray $S1$. For values of $n \sim 7$, the $S1$ area grows.

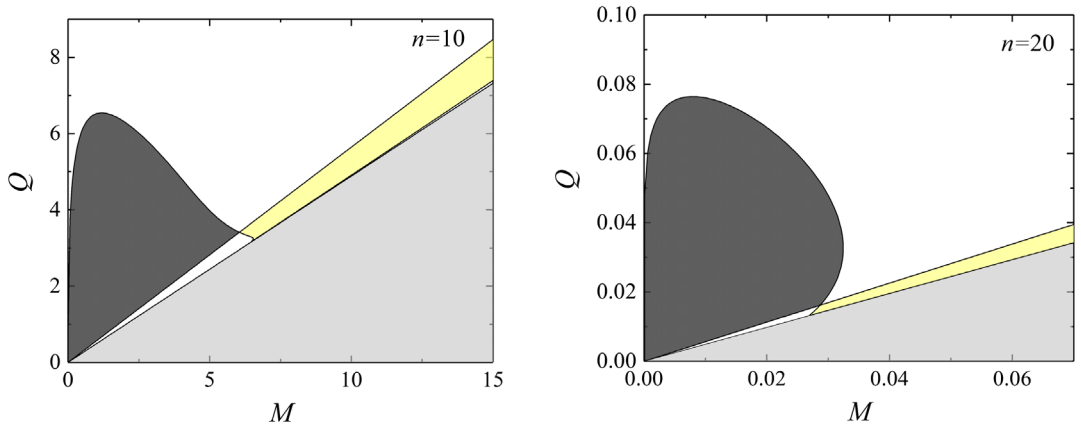

FIG. 7. For larger $n \gtrsim 7$, the black region ($S1$) shrinks to the origin and $S2$ dominates.

distribution of radiating matter over the disk. We estimated the surface brightness within the Page-Thorne model [56] showing that there is an increase in the radiation flux from the innermost region with small radii under the assumption of the fixed rest mass accretion rate[2] $\dot{M}_0$—similar to the results of [31,33] on the FJNW solution. However, in case of the SCO distribution, with several nonconnected rings, the (unknown) value of $\dot{M}_0$ may be very different for outer and inner rings: One can expect that the rest mass inflow to the inner ring may be much less than to the outer ring due to the scattering of the incoming material. This requires a significant modification of the AD model, presumably within the framework of hydrodynamic modeling, which is beyond the scope of this article. In this view, we limited ourselves to show the observed contours of the SCO regions for accretion disks and the frequency distributions over these disks due to the gravitational redshift and the Doppler effects.

To plot the SCOD images as seen by a distant observer, we need the trajectories of photons falling from infinity. Their properties depend on the sign of $\eta - 3$. For $\eta > 3$, when there is maximum of $U_{\rm eff}$, then the incoming photons with impact parameter $\lambda < [b_{\rm max}]^{-1/2}$, where $b_{\rm max} = \exp[\alpha(r_{\rm ph})]/r_{\rm ph}^2$, will reach singularity at the origin (see the left panel of Fig. 13). For $\eta < 3$, the photons with a nonzero angular momentum will be reflected from the potential (right panel of Fig. 13). Due to the strong bending of the rays, a scattered photon can hit a point on the AD plane far enough from the center, where another photon with a different trajectory also hits. Each such point has two images. On the other hand, there are no photons falling into the AD region near the singularity; this area is not visible to a distant observer.

The photon trajectories needed in the ray-tracing method were obtained numerically, similar to those shown in Fig. 13. We fix a sufficiently large distance to the static observer, where the geometry can be considered flat, and

[2]In the Page-Thorne model, the rest mass accretion rate $\dot{M}_0 \equiv dM_0/dt$ is defined as time-averaged rate at which the rest mass flows inward through the disk [56].

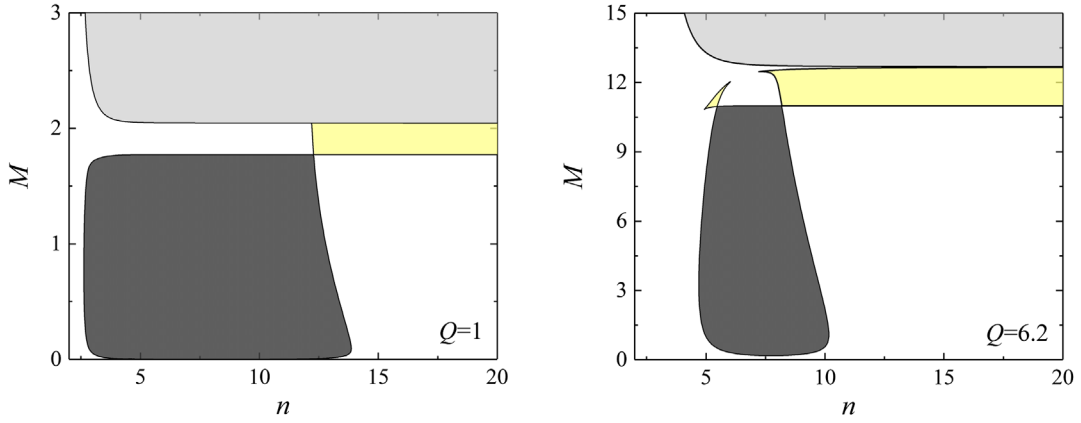

FIG. 8. Domains of parameters on the (n, M) plane for different values of Q.

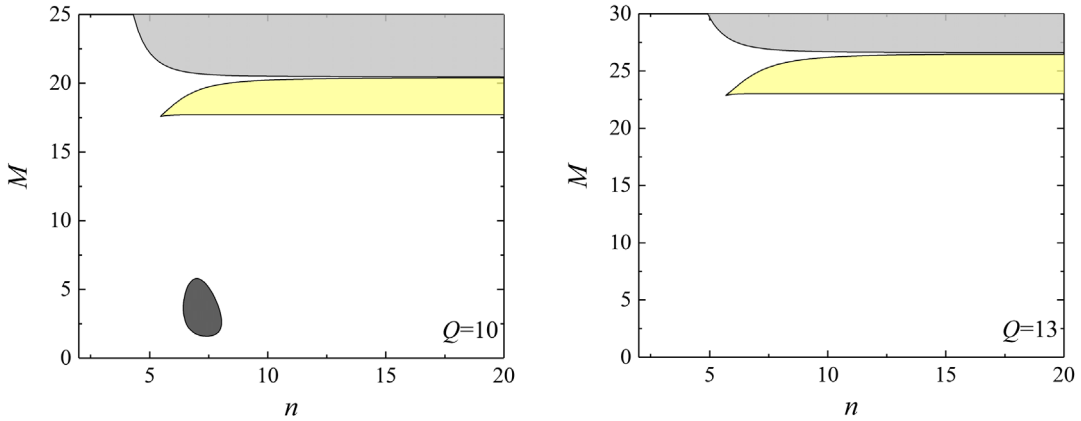

FIG. 9. The same as on the previous figure for larger Q.

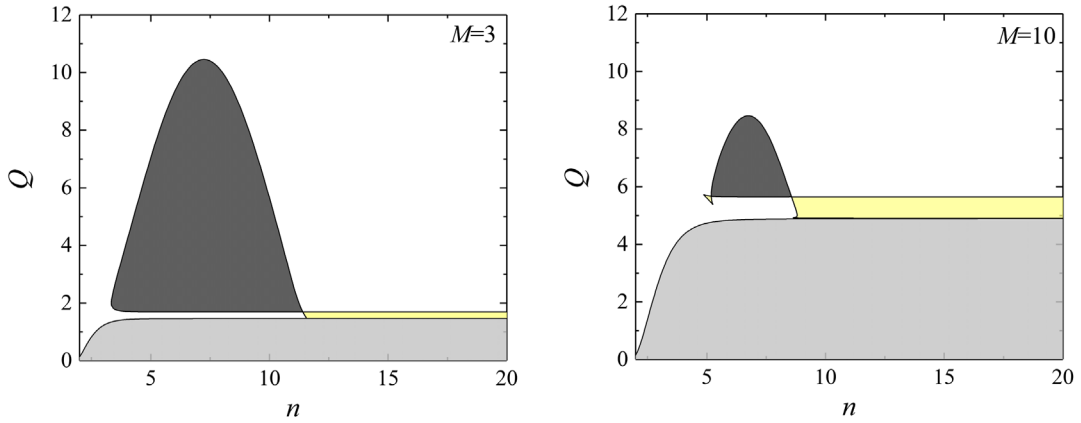

FIG. 10. Domains of parameters on (n, Q) plane for different values of M.

we track the photons coming from the observer to the AD plane, where we take into account only those photons that hit the SCO regions; also, we assume that the singularity itself does not radiate. We do not take into account the input from the reverse side of AD. The frequency ratio g between the point (e) at the AD surface and static remote observer (o) for metric (1) is

$$g = \frac{k_\mu u^\mu|_o}{k_\mu u^\mu|_e} = \frac{\sqrt{e^{\alpha(r)} - r^2\Omega^2}}{1 + \lambda\Omega}. \tag{19}$$

This formula takes into account both gravitational and Doppler effects. We use the normalized redshift factor,

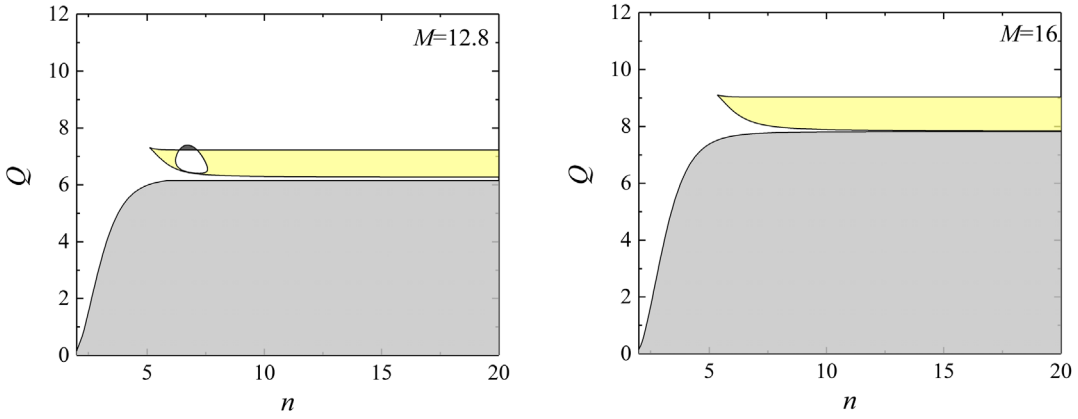

FIG. 11. The same as on the previous figure for larger M. For arbitrary M, there is a domain on (n, Q)-plane where $S3$ type exists.

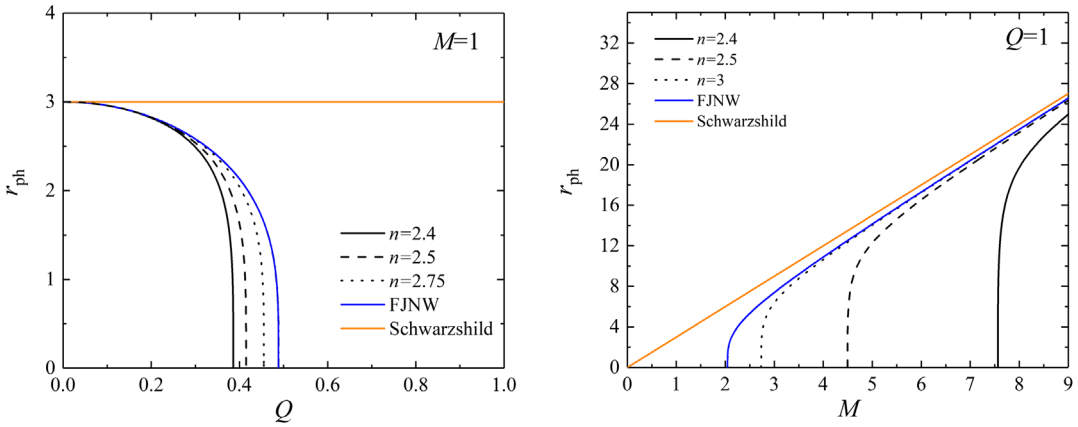

FIG. 12. The photon orbits radii as a function of scalar charge Q (left) and configuration mass M (right) for different values of n. Blue and orange curves correspond to the cases of FJNW and Schwarzschild metrics. Curves $r_{\rm ph}$ go below FJNW and tend to them with increasing n.

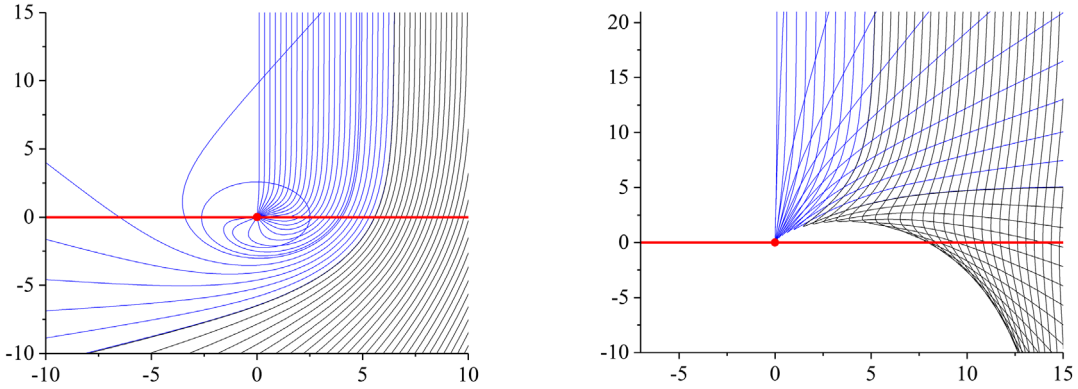

FIG. 13. In both panels $n = 3$, $M = 1$, the red line indicates the equatorial plane. Left: trajectories of photons incident from infinity to the attracting singularity; $Q = 0.3$, $\eta = 4.89$. Right: the same with the repulsing singularity $Q = 2.2$, $\eta = 2.33$; in this case, the points near the singularity form a dark spot around the center, imitating a black hole.

$$\tilde{g} = \frac{g - g_{\min}}{g_{\max} - g_{\min}}, \tag{20}$$

where $g_{\min}$ and $g_{\max}$ is the minimal and maximal frequency ratios on disk, respectively.

Figures 14–21 show the SCOD contours and the distribution of $\tilde{g}$ over the image, visible from infinity. The common property of all the images is the existence of dark spot in the center like an ordinary black hole. This is either due to the properties of the photon trajectories falling from infinity ($\eta < 3$, when these photons cannot reach the region

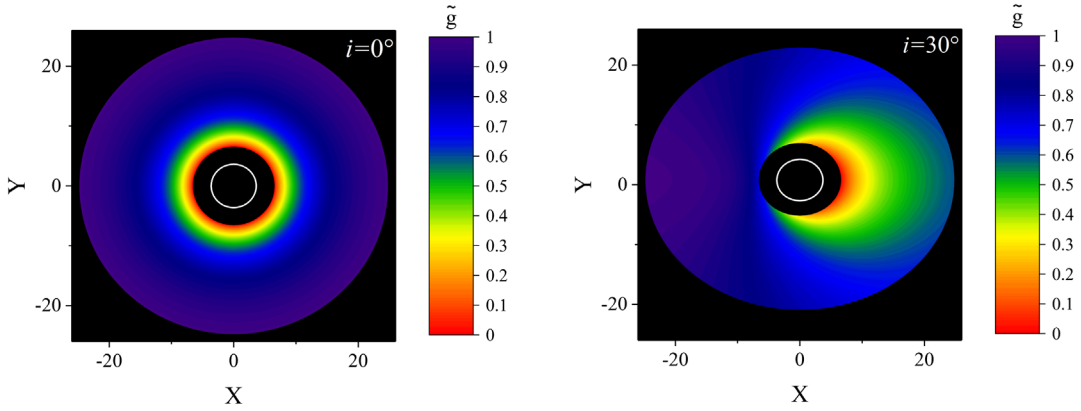

FIG. 14. AD images for the $U1$ type of SCOD ($M = 1$, $Q = 0.3$, $n = 3$): in full face and for inclination $i = 30°$. The white contour corresponds to the photon orbit at $r_{\rm ph} \approx 2.58$. The ISCO placed at $r_{1(U)} \approx 5.56$ and the outer disk edge was fixed at $r = 24$.

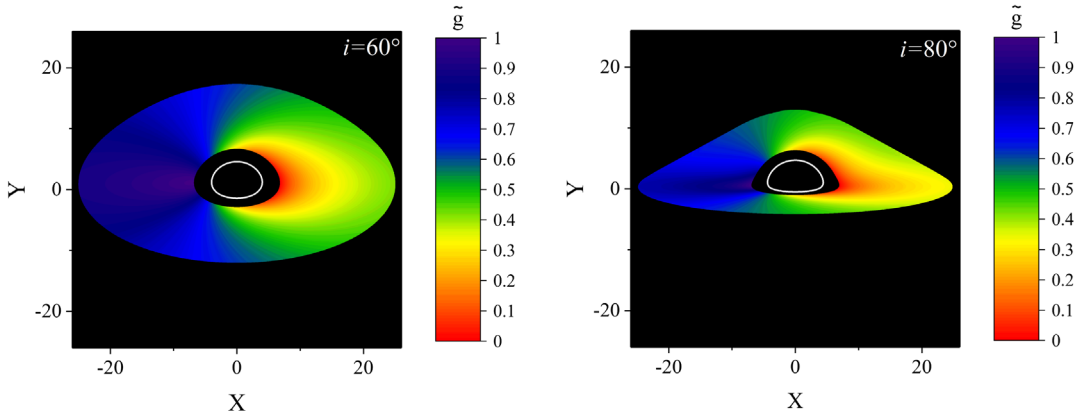

FIG. 15. The same as on Fig. 14 with inclinations 30° and 60°.

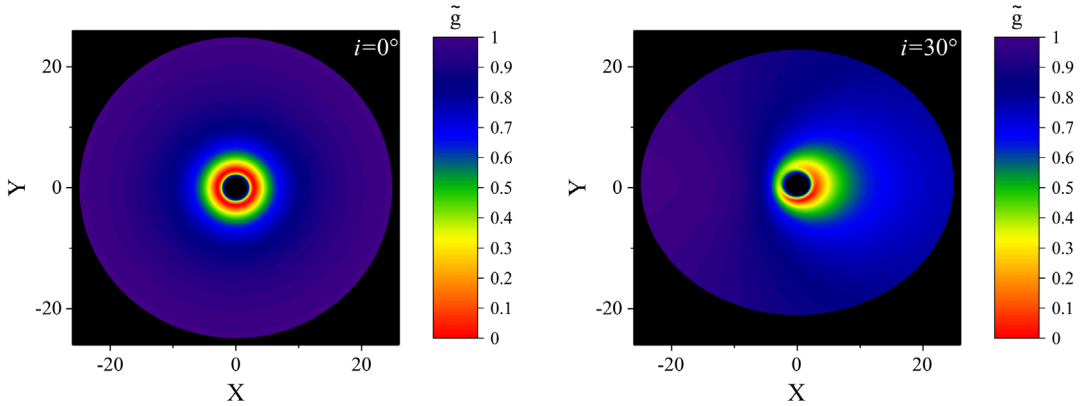

FIG. 16. AD images for the $S1$ type ($M = 1$, $Q = 0.8$, $n = 3$); in full face and for inclination $i = 30°$. The outer disk edge radius $r = 24$. There is a dark spot in the center due to the repulsive character of the naked singularity.

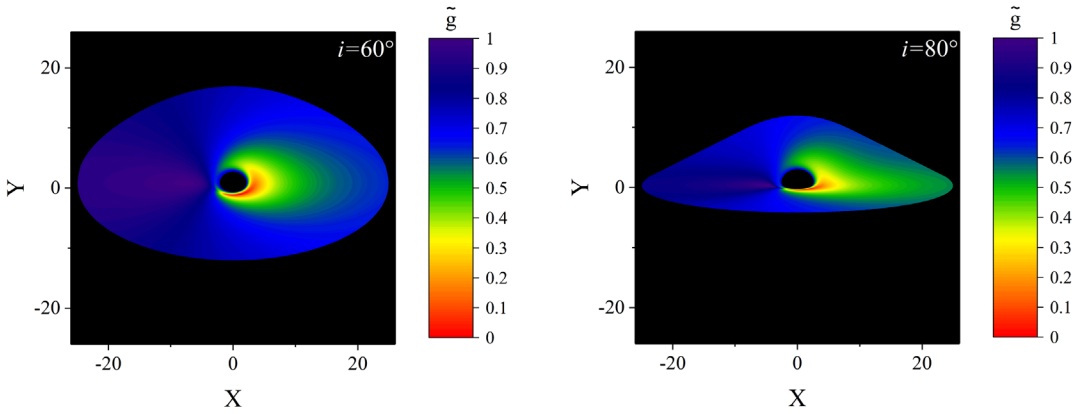

FIG. 17. The same as on Fig. 16 with inclinations 60° and 80°.

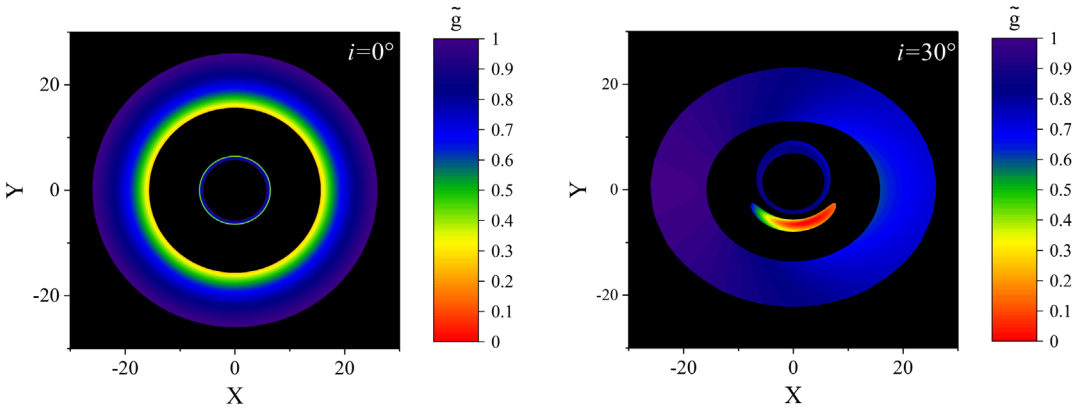

FIG. 18. AD images for the $S2$ type ($M = 1$, $Q = 2.2$, $n = 3$) in full face and for inclination $i = 30°$. The outer disk edge radius is $r = 24$. SCO radii are in intervals (i) $r \in (0, 6.5)$ and (ii) $r \in (14.5, \infty)$. However, the inner SCO region (i) cannot be observed in the left panel due to the repulsive nature of the naked singularity[a], but the inner ring in the left panel represents the secondary image of the outer part (ii) of the AD. The region (i) appears as the crescentlike feature on the right panel. [a] This does not mean that the region (i) cannot be observed from the other directions, e.g., if the disk is observed edge on.

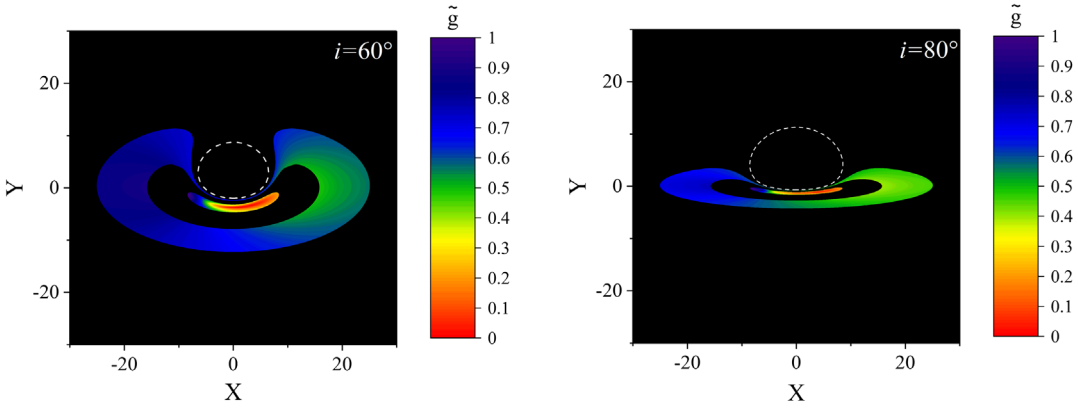

FIG. 19. The same as on Fig. 18 with inclinations 60° and 80°. The outer disk edge is $r = 24$. The white dashed line here shows the outline of the shadow of the naked singularity when it is illuminated by background light.

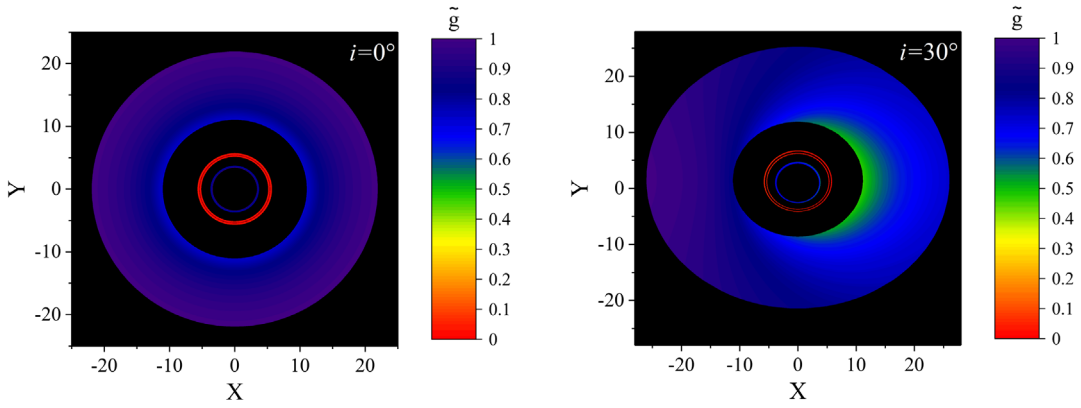

FIG. 20. AD images for the $S3$ type ($M = 2$, $Q = 0.99$, $n = 14$), $\eta \approx 2.9998$, in full face and for inclination $i = 30°$. The outer disk edge radius is $r = 24$. SCO radii intervals are (i) $r \in (0, 0.22)$—inner SCO region, (ii) $r \in (0.65, 2.14)$—intermediate SCO ring, and (iii) $r \in (9, \infty)$—outer unbounded SCO ring. The dark blue rings in the centers represents the secondary image of the outer disk; because of strong lensing effect, it has high surface brightness. The intermediate SCO ring (ii) has two images represented by two red circles that almost merge together. The inner SCO region (i) is invisible in both panels.

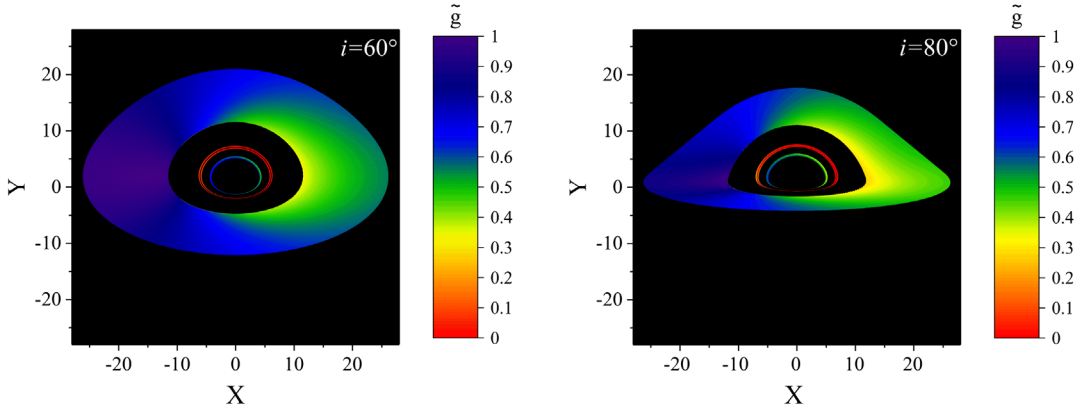

FIG. 21. The same as on Fig. 20 with inclinations 60° and 80°.

near the center), or simply because of absence of SCO in this region.

IV. DISCUSSION

We have studied isolated static spherically symmetric configurations of general relativity with minimally coupled nonlinear SF. The nonlinearity is introduced due to the SF potential $V(\phi) = \phi^{2n}$. For fixed $n > 2$, we have shown that the solution of the corresponding Einstein-SF system of equations exists and is unique under the appropriate conditions at spatial infinity describing an isolated object. This means that the configuration with the scalar field is uniquely defined by two parameters: the configuration mass M and the scalar charge Q defined from the SF asymptotics $\phi(r) \approx Q/r$ for $r \to \infty$. There is a naked singularity at the center; the asymptotic behavior of the solutions in its neighborhood depends on parameter η, which describes the type of the singularity and defines the asymptotic behavior of the effective potential for $r \to 0$. There is a critical value $\eta = 3$ that separates two types of singularity—attractive and repulsive—with different behavior of null geodesics near the center.

The solutions of the Einstein-SF system have been investigated numerically up to $n \sim 40$ for sufficiently large $M \sim 60$ and $Q \sim 60$. There are a lot of new elements in comparison with the FJNW solution, which arise in the dependencies of SCOD characteristics on configuration parameters. The most important difference from FJNW is associated with the emergence of the $S3$-type of SCOD with two rings of unstable circular orbits for $n \gtrsim 4.3$ for certain M, Q. Indeed, though stable circular geodesics represent a very simplified model [56] of an accretion disk, the above stability properties may be important for real AD.

We found 4 SCOD types, three of which are possible in the FJNW case. The $U1$ type is similar to the SCO distribution in the case of the Schwarzschild metric: There is an inner region around the center where circular orbits either do not exist, or are unstable, and there is an outer region of SCO that extends to infinity. For $S1$ type,

SCOs fill all the space starting from the center. For $S2$ type the stable orbits near the center are separated by a ring of unstable orbits from the outer SCO region that extends to infinity. Correspondingly, the images of the thin accretion disks are qualitatively similar to the FJNW case. And, at last, there is a new type ($S3$) with an additional SCO region and with two rings of the unstable circular orbits that separate SCO rings. Possible cases of SCOD are presented in Figs. 6 and 7 for different domains on the plane of the configuration parameters M, Q. One can infer that the $S3$ type is less probable; moreover, the innermost SCO rings typically have rather small radii for moderate M, Q.

We plotted the observable contours of the accretion disks of the same radius and images of SCO regions using the ray-tracing algorithm [58–60]. Figures 14–21 also show the redshift distribution over AD image, which may be useful to study deformation of the relativistic lines (e.g., Fe Kα) in the x-ray spectra of compact objects. A common feature of all the images is the dark spot in the center. This is either due to the absence of SCO near the center or because of strong bending of the photon trajectories near the naked singularity. In case of $S2$ and $S2$ types, Figs. 16–21 demonstrate bright subtle features around the center, which, in principle, can be observed in case of a good resolution. Also, these features can manifest themselves in microlensing events, provided that the configuration is the source of the gravitational lens system. However, these features were not observed by EHT [6] for M87*. Apparently, these types should be ruled out in case of M87*, though (i) observations with better resolution are desirable to have a final answer; (ii) comparison with [6] must take into account effects of rotation of the central object; i.e., there is a need to go beyond spherical symmetry; and (iii) a more sophisticated AD model is needed. This deserves a separate consideration.

To sum up, we note that basic qualitative properties of static spherically symmetric solutions of the Einstein-SF equations with monomial potential (3) have much in common with the linear massless FJNW case [7,8]. However, there are subtle details in the distribution of matter around the configuration, which distinguish the case of the nonlinear SF.

ACKNOWLEDGMENTS

O. S. S. and V. I. Z. acknowledge the support from National Research Foundation of Ukraine (Project No. 2020.02/0073). The work of A. N. A. has been supported by a scientific program "Astronomy and space physics" of Taras Shevchenko National University of Kyiv (Project No. 19BF023-01).

APPENDIX: ITERATION METHOD FOR SOLUTIONS AT LARGE DISTANCES

A consideration of existence and uniqueness for an isolated configuration in the asymptotically flat space-time has been carried out in our paper [61], where we have used the so called "quasi-global" coordinates. Here, we present a direct proof in the coordinate system defined by the metric representation (1).

We introduce variables,

$$X(r) = r(e^{-\beta} - 1), \qquad Y(r) = r^2 e^{\frac{\alpha-\beta}{2}} \frac{d\phi}{dr}.$$

The asymptotic flatness conditions, (7) and (8), can be rewritten in terms of X, Y, α, ϕ as

$$\lim_{r\to\infty} X(r) = -r_g, \qquad \lim_{r\to\infty} Y(r) = -Q,$$
$$\lim_{r\to\infty} [r\alpha(r)] = -r_g. \tag{A1}$$

From (8), we also have

$$\lim_{r\to\infty} [r\phi(r) - Q] = -\lim_{r\to\infty} r \int_r^\infty \frac{x^2 d\phi/dx + Q}{x^2} = 0,$$

and then

$$\lim_{r\to\infty} [r\phi(r)] = Q. \tag{A2}$$

Einstein Eqs. (4) and (5) and SF Eq. (6) can be rewritten in terms of $Z \equiv \{X, Y, \alpha, \phi\}$ as the first order system.

Equations (4) and (6) yield

$$\frac{dX}{dr} = -8\pi \left[e^{-\alpha} \frac{Y^2}{2r^2} + r^2 |\phi|^{2n} \right], \tag{A3}$$

$$\frac{dY}{dr} = 2nr^2 e^{\alpha/2} \frac{\phi|\phi|^{2n-2}}{\sqrt{1 + X/r}}. \tag{A4}$$

In Eq. (5), that takes the form,

$$\frac{d\alpha}{dr} = \frac{1}{1 + X/r} \left\{ -\frac{X(r)}{r^2} + 8\pi r \left[e^{-\alpha} \frac{Y^2}{2r^4} - |\phi|^{2n} \right] \right\}.$$

We separate out the dominating term for $r \to \infty$:

$$\frac{d\alpha}{dr} = \frac{r_g}{r^2(1 - r_g/r)} + D(Z, r), \tag{A5}$$

where

$$D(Z,r) = \frac{1}{1+X/r} \left\{ -\frac{X + r_g}{r^2(1-r_g/r)} + 8\pi r \left[e^{-\alpha} \frac{Y^2}{2r^4} - |\phi|^{2n} \right] \right\}. \tag{A6}$$

In the equation for $d\phi/dr$, which is expressed by means of Y,

$$\frac{d\phi}{dr} = e^{-\alpha/2}\frac{Y}{r^2\sqrt{1+X/r}},$$

we also separate out the dominating term:

$$\frac{d\phi}{dr} = -\frac{Q}{r^2\sqrt{1-r_g/r}} + E(Z,r), \tag{A7}$$

where

$$E(Z,r) = e^{-\alpha/2}\frac{Y}{r^2\sqrt{1+X/r}} + \frac{Q}{r^2\sqrt{1-r_g/r}}$$
$$= \frac{Y(e^{-\alpha/2}-1)}{r^2\sqrt{1+X/r}} + \frac{Q(X+r_g)}{r^3(\sqrt{1-r_g/r}+\sqrt{1+X/r})\sqrt{1-r_g/r}\sqrt{1+X/r}} + \frac{Y+Q}{r^2\sqrt{1+X/r}}.$$

Consider set $\mathbf{S}$ of continuous vector-functions $Z(r) = \{X(r), Y(r), \alpha(r), \phi(r)\}$, satisfying

$$|X(r)| \le 2r_g, \qquad |\alpha(r)| \le 2r_g/r, \qquad |Y(r)| \le 2|Q|,$$
$$|\phi(r)| \le 2|Q|/r, \qquad r \in [r_{\rm in}, \infty), \tag{A8}$$

where $r_{\rm in} > 0$ will be further assumed to be sufficiently large.

We shall construct a system of integral equations for solutions from $\mathbf{S}$, which is equivalent to equations [Eqs. (A3)–(A5) and (A7)] with conditions (A1). For the estimates below, it is essential that $n > 2$; the case $n = 2$ needs a separate consideration[3] not presented here.

Given the conditions (A1) and (A2), we get following system.

Equations (A3) and (A4) yield

$$X(r) = -r_g + A_1(Z,r),$$
$$A_1(Z,r) \equiv 8\pi\int_r^\infty ds\left[\frac{Y^2(s)}{2s^2}e^{-\alpha(s)} + s^2|\phi(s)|^{2n}\right], \tag{A9}$$

where we take into account $n > 2$;

$$Y(r) = -Q + A_2(Z,r),$$
$$A_2(Z,r) \equiv -2n\int_r^\infty ds\exp[\alpha(s)/2]\frac{s^2\phi(s)|\phi(s)|^{2n-2}}{\sqrt{1+X(s)/s}}. \tag{A10}$$

Equations (A5) and (A7) yield

$$\alpha(r) = \alpha_0(r) + A_3(Z,r),$$
$$\alpha_0(r) = \ln(1-r_g/r),$$
$$A_3(Z,r) \equiv -\int_r^\infty D(Z,s)ds; \tag{A11}$$

$$\phi(r) = \phi_0(r) + A_4(Z,r), \quad \phi_0(r) = \frac{2Q}{r_g}\left[1-\sqrt{1-r_g/r}\right],$$
$$A_4(Z,r) \equiv -\int_r^\infty E(Z,s)ds. \tag{A12}$$

Here, integral operators A_i, $i = 1,\ldots,4$, are defined on $\mathbf{S}$.

Let $Z(r) \equiv \{X(r), Y(r), \alpha(r), \phi(r)\} \in \mathbf{S}$. Denote

$$\tilde{X}(r) = -r_g + A_1(Z,r), \quad \tilde{Y}(r) = -Q + A_2(Z,r). \tag{A13}$$

For sufficiently large r, simple estimates on account of (A8) and $n > 2$ yield

$$|\tilde{X}(r) + r_g| = |A_1(Z,r)| \le \frac{C_1}{r},$$
$$|\tilde{Y}(r) + Q| = |A_2(Z,r)| \le \frac{C_3}{r^{2n-4}}. \tag{A14}$$

Here and below $C_i = C_i(M,Q)$, $i = 1,2,\ldots$ are finite positive constants. For sufficiently large r inequalities, (A8) and (A14) yield $|\tilde{X}(r)| \le 2r_g$, $|\tilde{Y}(r)| \le 2|Q|$; whence $Z' \equiv \{\tilde{X}(r), \alpha(r), \tilde{Y}(r), \phi(r)\} \in \mathbf{S}$.

Now, we denote

$$\tilde{\alpha}(r) = \alpha_0(r) + A_3(Z',r),$$
$$\tilde{\phi}(r) = \phi_0(r) + A_4(Z',r). \tag{A15}$$

Note that here we use Z' instead of Z and correspondingly $\tilde{X}$, $\tilde{Y}$ from (A13) instead of X, Y, which modifies the iteration scheme below. This provides some technical convenience in view of the specific form of the equations involved and allows us to avoid more stringent assumptions on $\mathbf{S}$. Using (A8) and (A14), for $n > 2$, we have

$$|r\tilde{\alpha}(r) + r_g| = |rA_3(Z',r)| \le \frac{C_4}{r}, \tag{A16}$$

and

[3]This can be done in a similar way, but more cumbersome.

$$|r\tilde{\phi}(r)+Q| = |rA_4(Z',r)| \le C_5\mu(r), \qquad \text{(A17)}$$

where $\mu(r)$ is defined immediately after formula (10).

Whence, for a sufficiently large r, $|\tilde{\alpha}(r)| < 2r_g/r$ and $|\phi(r)| < 2|Q|/r$ that is $\tilde{Z} \equiv \{\tilde{X}(r), \tilde{Y}(r), \tilde{\alpha}(r), \tilde{\phi}(r)\} \in \mathbf{S}$. Therefore, we have mapping $\mathbf{R}\colon Z \to \tilde{Z} = \mathbf{R}(Z)$ defined by (A13) and (A15), which transforms vector-function Z,

$$Z \to Z' \to \tilde{Z} = \{\tilde{X}(r), \tilde{Y}(r), \tilde{\alpha}(r), \tilde{\phi}(r)\} \in \mathbf{S};$$

i.e., (for sufficiently large r_{in}), operator $\mathbf{R}$ is correctly defined and maps functional class $\mathbf{S}$ into itself. Thus, initial equations are reduced to operator equation $Z = \mathbf{R}(Z)$.

Now, we proceed to estimate contraction mapping properties of $\mathbf{R}$. Let $Z_1 = \{X_1, Y_1, \alpha_1, \phi_1\} \in \mathbf{S}$, $Z_2 = \{X_2, Y_2, \alpha_2, \phi_2\} \in \mathbf{S}$; $\tilde{Z}_1 = \mathbf{R}(Z_1)$, $\tilde{Z}_2 = \mathbf{R}(Z_2)$; $\delta Z \equiv Z_1 - Z_2$.

Denote

$$\|Z\| \equiv \sup\{|X(r)| + r|\alpha(r)| + |Y(r)| + r|\phi(r)|, \quad r \in [r_{\text{in}}, \infty). \qquad \text{(A18)}$$

Equations (A13) on account of (A8) yield

$$|\delta\tilde{X}(r)| = |A_1(Z_1,r) - A_1(Z_2,r)| \le \frac{C_7}{r}\|\delta Z\|, \qquad \text{(A19)}$$

$$|\delta\tilde{Y}(r)| = |A_2(Z_1,r) - A_2(Z_2,r)| \le \frac{C_8}{r^{2n-4}}\|\delta Z\|. \qquad \text{(A20)}$$

Here and below, we systematically use the Lagrange finite-increments formula. Using explicit form (A6) of $D(X,r)$, we have

$$|D(Z_1,s) - D(Z_2,s)| \le \frac{C_9}{s^2}|\delta X(s)| + \frac{C_{10}}{s^3}|\delta Y(s)| + \frac{C_{11}}{s^4}(s|\delta\alpha(s)|) + \frac{C_{12}}{s^{2n-1}}(s|\delta\phi(s)|).$$

After substitution $Z_i \to \tilde{Z}_i$, $i = 1, 2$ on account of (A19) and (A20), we have

$$|D(Z_1',s) - D(Z_2',s)| \le \left\{\frac{C_9C_7}{s^3} + \frac{C_{11}}{s^4} + \frac{C_{10}C_8 + C_{12}}{s^{2n-1}}\right\}\|\delta Z\|,$$

whence

$$|\delta\tilde{\alpha}(r)| = |A_3(Z_1',r) - A_3(Z_2',r)| \le \frac{C_{13}}{r^2}\|\delta Z\|. \qquad \text{(A21)}$$

Analogously,

$$|E(Z_1,s) - E(Z_2,s)| \le \frac{C_{14}}{s^2}|\delta Y(s)|(1 + O(1/s)) + \frac{C_{15}}{s^4}|\delta X(s)| + \frac{C_{16}}{s^2}|\delta\alpha(s)|,$$

and then

$$|E(Z_1',s) - E(Z_2',s)| \le \frac{C_{14}C_8}{s^{2n-2}}\|\delta Z\|(1 + O(1/s)) + \frac{C_{15}}{s^4}|\delta X(s)| + \frac{C_{16}}{s^3}|s\delta\alpha(s)|),$$

$$|\delta\tilde{\phi}(r)| = |A_4(Z_1',r) - A_4(Z_2',r)| \le \frac{C_{17}}{r}\mu(r)\|\delta Z\|. \qquad \text{(A22)}$$

At last,

$$\|\mathbf{R}(Z') - \mathbf{R}(Z)\| \le \max\left[\frac{C_{16}}{r_{\text{in}}}, \frac{C_{17}}{r_{\text{in}}^{2n-4}}\right]\|\delta Z\|,$$

and we see that, for a sufficiently large r_{in}, $\mathbf{R}$ is contraction mapping. The solution can be obtained by successive approximations $Z_{(n+1)} = \mathbf{R}(Z_{(n)})$ with zeroth iteration $Z_{(0)} = \{-r_g, -Q, \alpha_0, \phi_0\}$. Leaving the main terms for large r, from the first iteration, we have

$$X_{(1)}(r) = -r_g + \frac{4\pi Q^2}{r}\{1 + O[\mu(r)]\}; \qquad \text{(A23)}$$

$$Y_{(1)}(r) = -Q - \frac{nQ|Q|^{2n-2}}{(n-2)r^{2n-4}}\{1 + O[\mu(r)]\}; \qquad \text{(A24)}$$

$$\alpha_{(1)}(r) = \alpha_0 + O\left[\frac{\mu(r)}{r^2}\right]; \qquad \text{(A25)}$$

$$\phi_{(1)}(r) = \frac{Q}{r}\left\{1 + \frac{r_g}{2r} + \frac{n|Q|^{2n-2}}{(n-2)(2n-3)r^{2n-4}}\right\} + O\left[\frac{\mu(r)}{r^2}\right]. \qquad \text{(A26)}$$

Here, we have left those orders in r^{-1} that will not change in subsequent iterations. These equations yield asymptotic relations (9) and (10).

[1] E. J. Copeland, M. Sami, and S. Tsujikawa, Int. J. Mod. Phys. D **15**, 1753 (2006).
[2] K. Bamba, S. Capozziello, S. Nojiri, and S. D. Odintsov, Astrophys. Space Sci. **342**, 155 (2012).
[3] B. Novosyadlyj, V. Pelykh, Y. Shtanov, and A. Zhuk, arXiv: 1502.04177.
[4] A. Linde, arXiv:1402.0526.
[5] E. D. Valentino, O. Mena, S. Pan, L. Visinelli, W. Yang, A. Melchiorri, D. F. Mota, A. G. Riess, and J. Silk, Classical Quantum Gravity **38**, 153001 (2021).
[6] K. Akiyama E. H. T. Collaboration, Astrophys. J. **875**, L1 (2019).
[7] I. Z. Fisher, Zh. Exp. Theor. Phys., **18**, 636 (1948).
[8] A. I. Janis, E. T. Newman, and J. Winicour, Phys. Rev. Lett. **20**, 878 (1968).
[9] M. Wyman, Phys. Rev. D **24**, 839 (1981).
[10] K. S. Virbhadra, Int. J. Mod. Phys. A **12**, 4831 (1997).
[11] J. D. Bekenstein, Phys. Rev. Lett. **28**, 452 (1972).
[12] J. D. Bekenstein, Phys. Rev. D **5**, 1239 (1972).
[13] D. D. Doneva and S. S. Yazadjiev, Phys. Rev. D **102**, 084055 (2020).
[14] R. Penrose, Phys. Rev. Lett. **14**, 57 (1965).
[15] R. Penrose, Gen. Relativ. Gravit. **34**, 1141 (2002).
[16] D. Christodoulou, Commun. Math. Phys. **93**, 171 (1984).
[17] A. Ori and T. Piran, Phys. Rev. Lett. **59**, 2137 (1987).
[18] P. S. Joshi and I. H. Dwivedi, Phys. Rev. D **47**, 5357 (1993).
[19] P. S. Joshi, D. Malafarina, and R. Narayan, Classical Quantum Gravity **31**, 015002 (2014).
[20] Y. C. Ong, Int. J. Mod. Phys. A **35**, 2030007 (2020).
[21] H. Olivares, Z. Younsi, C. M. Fromm, M. De Laurentis, O. Porth, Y. Mizuno, H. Falcke, M. Kramer, and L. Rezzolla, Mon. Not. R. Astron. Soc. **497**, 521 (2020).
[22] K. V. Aelst, E. Gourgoulhon, and F. H. Vincent, arXiv: 2103.01827.
[23] C. A. Herdeiro, A. M. Pombo, E. Radu, P. V. Cunha, and N. Sanchis-Gual, J. Cosmol. Astropart. Phys. 04 (2021) 051.
[24] A. B. Abdikamalov, A. A. Abdujabbarov, D. Ayzenberg, D. Malafarina, C. Bambi, and B. Ahmedov, Phys. Rev. D **100**, 024014 (2019).
[25] I. Banerjee, S. Chakraborty, and S. SenGupta, Phys. Rev. D **101**, 041301 (2020).
[26] I. Banerjee, S. Sau, and S. SenGupta, Phys. Rev. D **101**, 104057 (2020).
[27] S. Sau, I. Banerjee, and S. SenGupta, Phys. Rev. D **102**, 064027 (2020).
[28] F. H. Vincent, M. Wielgus, M. A. Abramowicz, E. Gourgoulhon, J.-P. Lasota, T. Paumard, and G. Perrin, Astron. Astrophys. **646**, A37 (2021).
[29] P. Bambhaniya, A. B. Joshi, D. Dey, and P. S. Joshi, Phys. Rev. D **100**, 124020 (2019).
[30] R. Shaikh and P. S. Joshi, J. Cosmol. Astropart. Phys. 10 (2019) 064.
[31] G. Gyulchev, P. Nedkova, T. Vetsov, and S. Yazadjiev, Phys. Rev. D **100**, 024055 (2019).
[32] G. Gyulchev, J. Kunz, P. Nedkova, T. Vetsov, and S. Yazadjiev, Eur. Phys. J. C **80**, 1017 (2020).
[33] A. N. Chowdhury, M. Patil, D. Malafarina, and P. S. Joshi, Phys. Rev. D **85**, 104031 (2012).
[34] S. Zhou, R. Zhang, J. Chen, and Y. Wang, Int. J. Theor. Phys. **54**, 2905 (2015).
[35] D. Pugliese, H. Quevedo, and R. Ruffini, Phys. Rev. D **83**, 024021 (2011).
[36] D. Pugliese, H. Quevedo, and R. Ruffini, Phys. Rev. D **88**, 024042 (2013).
[37] P. Slaný and Z. Stuchlík, Eur. Phys. J. C **80**, 587 (2020).
[38] Z. Stuchlík and J. Schee, Int. J. Mod. Phys. D **24**, 1550020 (2015).
[39] I. Dymnikova and A. Poszwa, Classical Quantum Gravity **36**, 105002 (2019).
[40] R. S. Vieira, J. Schee, W. Kluźniak, Z. Stuchlík, and M. Abramowicz, Phys. Rev. D **90**, 024035 (2014).
[41] O. S. Stashko and V. I. Zhdanov, Gen. Relativ. Gravit. **50**, 105 (2018).
[42] Z. Meliani, F. H. Vincent, P. Grandclément, E. Gourgoulhon, R. Monceau-Baroux, and O. Straub, Classical Quantum Gravity **32**, 235022 (2015).
[43] Z. Stuchlík and J. Schee, Classical Quantum Gravity **31**, 195013 (2014).
[44] J. Schee and Z. Stuchlík, Classical Quantum Gravity **33**, 085004 (2016).
[45] Z. Stuchlík, J. Schee, and D. Ovchinnikov, Astrophys. J. **887**, 145 (2019).
[46] S. Paul, R. Shaikh, P. Banerjee, and T. Sarkar, J. Cosmol. Astropart. Phys. 03 (2020) 055.
[47] S. Shahidi, T. Harko, and Z. Kovács, Eur. Phys. J. C **80**, 162 (2020).
[48] L. G. Collodel, D. D. Doneva, and S. S. Yazadjiev, Astrophys. J. **910**, 52 (2021).
[49] T. L. Smith, V. Poulin, and M. A. Amin, Phys. Rev. D **101**, 063523 (2020).
[50] S. Antusch, D. G. Figueroa, K. Marschall, and F. Torrenti, Phys. Lett. B **811**, 135888 (2020).
[51] M. Ballardini, D. Sapone, C. Umiltà, F. Finelli, and D. Paoletti, J. Cosmol. Astropart. Phys. 05 (2019) 049.
[52] V. I. Zhdanov and O. S. Stashko, Phys. Rev. D **101**, 064064 (2020).
[53] G. Stephenson, Math. Proc. Cambridge Philos. Soc. **58**, 521 (1962).
[54] R. A. Asanov, Theor. Math. Phys. **20**, 667 (1974).
[55] O. S. Stashko and V. I. Zhdanov, Ukr. J. Phys. **64**, 1078 (2019).
[56] D. N. Page and K. S. Thorne, Astrophys. J. **191**, 499 (1974).
[57] O. Stashko and V. Zhdanov, Ukr. J. Phys. **64**, 189 (2019).
[58] D. Psaltis and T. Johannsen, Astrophys. J. **745**, 1 (2012).
[59] T. Johannsen and D. Psaltis, Astrophys. J. **718**, 446 (2010).
[60] C. Bambi, Astrophys. J. **761**, 174 (2012).
[61] A. Alexandrov, O. Stashko, and V. Zhdanov, Bull. Taras Shevchenko Natl. Univ. Kyiv Astron. **59**, 6 (2019).